



The autonomous robotic environmental sensor (ARES)

Benjamin Dyer, Mohammad Biglarbegian & Amir A. Aliabadi

To cite this article: Benjamin Dyer, Mohammad Biglarbegian & Amir A. Aliabadi (2021) The autonomous robotic environmental sensor (ARES), Science and Technology for the Built Environment, 27:10, 1461-1472, DOI: [10.1080/23744731.2021.1971034](https://doi.org/10.1080/23744731.2021.1971034)

To link to this article: <https://doi.org/10.1080/23744731.2021.1971034>



Published online: 07 Sep 2021.



Submit your article to this journal [↗](#)



Article views: 90



View related articles [↗](#)



View Crossmark data [↗](#)



The autonomous robotic environmental sensor (ARES)

BENJAMIN DYER, MOHAMMAD BIGLARBEKIAN and AMIR A. ALIABADI* 

School of Engineering, University of Guelph, Guelph, ON, N1G 2W1, Canada

Measurement of thermal comfort in the indoor environment enables making adjustments to building design and operations to improve building performance. Methods of measurement tend to be tedious and expensive, requiring several expensive sensors to be mounted in the building. In this paper, we propose the Autonomous Robotic Environmental Sensor (ARES), a custom-designed omniwheel mobile robot retrofitted with several sensors capable of autonomously taking measurements of the indoor environment at multiple positions, reducing the number of sensors, amount of labor required, and cost. A Sliding Mode Controller (SMC) is designed and applied to the robotic platform, and positional accuracy is verified, allowing for highly accurate movement to ensure environmental measurements occur at known positions. Wind velocity, air temperature, and relative humidity data collected by the ARES platform in a laboratory environment for 24 hours is analyzed, providing insight into the thermo-fluid variables in the room and the room's predicted thermal comfort.

Introduction

Large buildings occasionally have issues with their indoor environment due to fluctuations in personnel, large floor areas, complex airflow, and long operational time (Gärtner, Massa Gray, and Auer 2020; Reena, Mathew, and Jacob 2018). These will result in uneven heating and cooling throughout the building and within large rooms causing occupants to feel uncomfortably hot or cold depending on their location and the time of day (Fan 2019). To combat poor indoor conditions, it is important to predict and adapt the environmental parameters such as temperature, moisture, etc. to meet its occupants' needs. Therefore, low-cost, novel solutions should be developed to collect data in the indoor environment efficiently.

Indoor environmental sensing

Indoor environmental sensing falls into three categories: static sensor stations, wearable sensors, and mobile sensing. Static sensors are the most commonly used as they allow for measurement of the environment at different locations in a building and require little oversight after being set up. In an ideal world, a dense sensor network can be assembled,

resulting in highly accurate spatial and temporal measurements of the environment; however, dense sensor networks can interfere with occupants using the space, often limiting sensors to low-traffic areas of the building. In addition, dense sensor networks are prohibitively expensive both in setup and maintenance, depending on sensor type (Williams 2019; Caubel, Cados, and Kirchstetter 2018). Therefore, it is desirable to collect this data using non-intrusive and low-cost methods. Placement requirements of static sensors can be loosened by combining collected data with Computation Fluid Dynamics (CFD) simulations or other modeling methods.

CFD simulations have been used extensively to predict thermal fields, airflow patterns, concentration distributions of gasses and particulates, and prediction of thermal comfort (Nielsen 2015; Zhao, Li, and Yan 2003). However, a major drawback of CFD is the reliance on initial and boundary conditions, particularly wall surface temperatures, air inlet temperatures, and inlet and outlet airflow rates (Aliabadi, Veriotes, and Pedro 2018). Small differences in these conditions can significantly change the results of simulations, with acceptable results still producing errors upwards of 20% (Posner, Buchanan, and Dunn-Rankin 2003). Therefore, the combination of static sensors with numerical simulation methodologies can produce more accurate results by using collected data as boundary conditions or for verification purposes for the simulations (Shan and Lu 2021). However, CFD calculations are complex, require computing facilities, and are often beyond the skills of the most practical engineers (Aliabadi et al. 2011), increasing the cost of accurately predicting the environment where static sensors cannot be deployed.

Received: 8 January 2021; Accepted: 16 August 2021

Benjamin Dyer, MASC, is a Student at the School of Engineering. **Mohammad Biglarbekian, PhD, PEng**, is an Associate Professor at the School of Engineering. **Amir A. Aliabadi, PhD, PEng**, is an Associate Professor at the School of Engineering.

*Corresponding author e-mail aliabadi@uoguelph.ca

Wearable sensors provide an easy method to measure environmental variables over large areas at a relatively low cost, causing a recent increase of interest for person-based sensing devices (Wilson 2019). While often used for monitoring personal health, wearable sensors are effective at measuring environmental variables such as pollutant concentrations, air temperature and humidity, harmful radiation, and noise. However, wearable sensors have difficulties measuring environmental variables such as long and short-wave radiation or wind speed due to inconsistent orientation and lack of sensor miniaturization (ISO standard 2017). Additionally, in the indoor environment, variables such as PM_{2.5} (particulate matter with a diameter less than 2.5 µm) levels and temperatures can change rapidly between rooms, requiring the time constant of the sensors to be on the order of 10 s or less, reducing measurement accuracy (Schlink and Ueberham 2021; Rabinovitch et al. 2016). While wearable sensors are useful for measuring the local environment, they provide little control over measurement locations, requiring many personal sensors to adequately measure a large indoor environment (Schlink and Ueberham 2021). A convenient middle ground between wearable and static sensors are mobile sensing platforms that can measure the environment at desired locations at a fraction of the cost of static sensors.

Mobile environmental sensing

In recent years, mobile sensing in the indoor environment has often been focused on measurement and localization of airborne contaminants through olfaction (Chen et al. 2017; Feng et al. 2019). Heinzerling et al. (2013) reviewed several mobile sensing carts, which featured different sensor configurations for determining Indoor Environmental Quality (IEQ). These carts can be moved around a building and left to take measurements at any position; however, they require human intervention to change measurement positions. Operational cost can be reduced by mounting sensor arrays on an autonomous robot, as is typical for contaminant localization (Jin et al. 2018).

Several mobile sensing platforms have been developed previously; however, these platforms focus on a single type of measurement and are difficult to adapt to other measurement types. Lilienthal, Loutfi, and Duckett (2006) outfitted a Koala mobile robot with a mobile nose capable of traversing an indoor environment to build an accurate gas concentration grid map. Yang et al. (2019) also developed a mobile sensing platform to perform gas source localization in an indoor environment and quantified performance of multiple olfaction algorithms. Feng et al. (2019) built three mobile robots using the TurtleBot2 as the base platform for multiple-robot contamination source localization. These mobile robots are effective at their tasks; however, they lack modularity making it difficult to quickly change sensors and repurpose the platforms for different types of sensing. Jin et al. (2018) developed a more modular mobile platform utilizing the TurtleBot2 as the mobile base and a Kinect camera for localization. The use of the Kinect camera enables a low-cost localization method but significantly increases power

consumption which would interfere with some measurements, such as temperature, humidity, and wind velocity vector components. Additionally, increased power consumption results in shorter operational times between charging or discharging batteries.

All previously-discussed mobile sensing platforms utilize a differential drive system (Jin et al. 2018; Lilienthal, Loutfi, and Duckett 2006; Yang et al. 2019). Differential drive systems are capable of rotating without translating allowing navigation of tight spaces often encountered indoors (Phillis 2008). However, differential drive designs suffer from the need to always align the robot in the direction of motion, requiring the robot to first rotate before translating. The reliance on rotation for translation introduces error in the positional accuracy of the robot since small errors in angular position result in large errors in position over medium to long travel distances. Normally, this problem is solved using localization systems, which increase system cost, complexity, and reduce the operational time due to high power consumption (Bi, Yang, and Cai 2018; Lee et al. 2020). It is possible to avoid rotation entirely using an omniwheel robot.

Omn wheel robots utilize three or more omniwheels, allowing holonomic motion. The Swedish omniwheel contains rollers equally distributed around the wheel to allow the wheel to translate perpendicular to its rotation. By positioning three or more omniwheels radially about the robot a holonomic configuration is obtained, allowing the robot to translate freely without rotation (Smith et al. 2020). Reduction in rotation allows for higher positional accuracy in medium to long distance translations and simpler path planning. Additionally, pathing can be made more efficient by having the robot rotate while translating.

Thermal comfort

Due to reliance on an individual's thermal sensations, thermal comfort is intrinsically subjective. The American Society of Heating, Refrigerating and Air-Conditioning Engineers (ASHRAE) has developed the ASHRAE thermal sensation scale to quantify thermal comfort. The scale ranges from -3 to 3 with 0 being a neutral sensation, negative values being cold, and positive values being hot (ASHRAE 2017). Normally thermal comfort would be quantified on the scale by surveying occupants of a building or deployment of personal measurement devices; however, it is often useful to estimate the average thermal sensation rating for an environment based on quantitative measurements of environmental physical variables.

To accomplish this, Fanger (1970) developed the widely used Predicted Mean Vote (PMV) and the Predicted Percent Dissatisfied (PPD) model. The PMV-PPD model uses four environmental variables (ambient air temperature, relative humidity, wind speed, and mean radiant temperature) and two physiological variables (metabolic rate and clothing insulation) to predict the average thermal comfort vote of a large group of people in a given environment. While environmental variables can be measured or estimated, physiological variables are determined using the ASHRAE thermal

comfort standard, which provides tables of metabolic rates and clothing levels during different activities and for different types of clothing (Fanger 1972). Mean Radiant Temperature (MRT) can be estimated based on the ambient air temperature since the MRT and ambient temperature have typically a mean difference within 0.3 K and a median absolute difference within 0.4 K. These differences are based on an analysis of the ASHRAE Global Thermal Comfort Database, five field studies, and five laboratory test conditions (Dawe et al. 2020; Földváry Ličina et al. 2018).

Objectives

To the best of the authors' knowledge, little to no prior work has been conducted in the development of a modular autonomous robotic platform to measure the indoor environment. Furthermore, omniwheel robots have not been used for autonomous environmental sensing, despite having some advantages over differential drive robots. In this paper an omniwheel mobile environmental sensing platform is developed and described in detail. A non-linear controller is developed to ensure the platform has high positional accuracy regardless of load. The platform is deployed in a laboratory environment over a diurnal cycle to showcase its capabilities. Data from the environment is analyzed for quantification of thermo-fluid variables and thermal comfort. Platform cost-effectiveness is discussed in comparison to static sensors, and measurement time guidelines are discussed.

Methodology

This section describes the methods used for controlling the Autonomous Robotic Environmental Sensor (ARES) and analyzing the collected data (i.e. environmental variables such as wind velocity, temperature, and relative humidity). The platform is described, and a control scheme based on a kinematic model is designed. Standard methods for obtaining variances and covariances of environmental variables, and their systematic and random errors are formulated. The Predicted Mean Vote (PMV)-Predicted Percent Dissatisfied (PPD) model is briefly described, and the error due to simplifications of the model is quantified. Finally, an environmental sensing experiment is formulated to determine environmental statistics and predicted thermal comfort in an indoor office environment.

Platform

ARES has three Swedish omniwheels in a rotationally symmetric pattern resulting in a holonomic platform capable of translating without rotation, as shown in Figure 1. The wheels are positioned radially about the robot, with each wheel 26.32 cm from the robot's center. The wheels are embedded to guarantee even ground contact, reducing risk of slippage and increasing maximum load. Each wheel is driven using a Pololu 37Dx73L DC motor with a maximum speed of 67 rpm and a maximum torque of 49 g cm. The

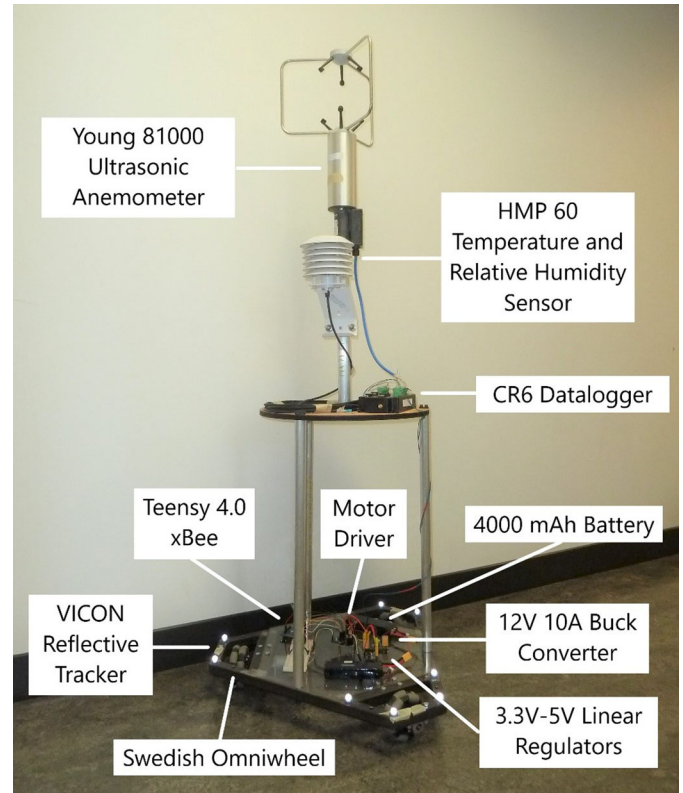


Fig. 1. ARES in the configuration used for environmental sensing.

omniwheels have a radius of 5.08 cm giving the robot a maximum speed of 30.8 cm s^{-1} . The robot's maximum speed is based on its orientation and can be as low as 17.8 cm s^{-1} . High resolution quadrature encoders are attached to the motor shaft providing 9600 encoder ticks per revolution resulting in a 0.15-degree resolution.

The robot consists of two main subsystems, the base, including all the hardware, and the sensor stack up, containing all the environmental sensors.

ARES base

The frame was designed using an equilateral triangle, with each side measuring 27.56 inches. The corners of the triangle were truncated such that there would be a 4.33-inch-long segment resulting in a hexagon with alternating 4.33-inch and 18.90-inch side lengths. Finally, three segments were added to the inside of the hexagon such that they were parallel to and 3 inches away from the 4.33-inch segments. The robot's outer segments were built using 1×1 -inch square iron tubing, and the inner segments were built using 2×1 -inch square iron tubing. All tubing was welded together to ensure the frame was rigid and robust. Mounting holes were drilled in the frame as needed.

The wheel drive, shown in Figure 2, is designed to carry a maximum load of 50 kg. The frame's design supports embedded wheels, allowing the wheels to be supported on both sides, resulting in high load capacity and accurate wheel alignment. A $1/4$ -inch D-shaft axle is aligned using

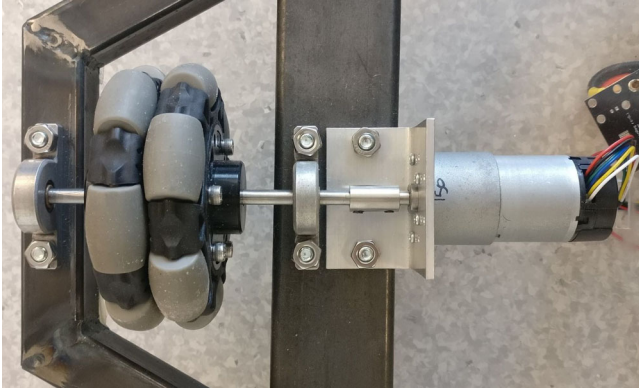


Fig. 2. View of a wheel drive from the bottom of the platform.

two oil-embedded bushings with self-alignment of 5 degrees, allowing for smooth axle rotation. The 4-inch omnivheels are attached to the axle using the appropriate wheel hubs (both acquired from Vex Robotics). Motor shaft adapters were machined to convert from the 6-mm motor D-shaft to the $\frac{1}{4}$ -inch axle. The motors are mounted to the frame using an $\frac{1}{8}$ -inch-thick piece of angle iron with a standard array of mounting holes drilled, allowing for the motor to be changed without disassembly of the whole wheel drive. All parts chosen have $\frac{1}{2}$ -inch variants, which support the same mounting holes allowing for the maximum load to be increased easily. Additionally, the frame supports 6-inch omnivheels if higher speed is desired without sacrificing torque.

An acrylic sheet was cut and mounted to the top side of the frame using the same mounting holes as the motor brackets. Mounting holes were drilled as needed into the acrylic sheet for mounting all electronics. The frame's design lends itself well to modularity as mounting holes up to $\frac{3}{8}$ -inches in diameter can be drilled into nearly any part of the frame without decreasing structural integrity. The wheel drive can be easily and quickly modified to change the wheel size, axle size, and the motor allowing for different top speeds and maximum loads.

Electrical system

Power delivery for both sub-systems is handled by two 4000 mAh 3S LiPo batteries configured in series providing an average 22.2 V at 30 A transient and 60 A peak. A custom-designed 12 V, 10 A buck converter based on the Analog Devices LTC3807 provides up to 120 W at 96% efficiency. The 12 V buck converter allows for a 42 V input for more batteries to be connected to the robot, extending the time between re-charging operations. In the current configuration the robot can perform sensing for 8 hours between charges, but the addition of larger batteries can extend operational time to more than 48 hours. For powering encoders and micro-controllers, 5 V and 3.3 V rails are produced using Texas Instrument LM1085 linear regulators powered using the 12 V rail. All electrical components were designed with low power consumption in mind to extend operational time and reduce heat generation.

The platform uses a Teensy 4.0 micro-controller as the processing power of the robot. The Teensy 4.0 communicates via serial to a Digi xBee wifi module, which is paired to another Digi xBee connected to a computer for sending desired positions to the robot. The micro-controller communicates with a custom motor driver board via an I²C bus, allowing the motor speeds to be set using a 12-bit PWM signal. Encoder ticks are counted by the Teensy 4.0 using interrupts after the 5 V encoder signals are shifted down to 3.3 V.

Sensor stack-up

Environmental sensors are mounted on a raised platform consisting of three 60 cm long, 2.54 cm diameter aluminum rods mounted directly through the robot frame. A circular piece of wood is attached to the top of the three rods providing a platform for the CR6 data logger (Campbell Scientific, Logan, Utah, USA). A 45 cm, 3.175 cm diameter aluminum rod is mounted at the center of the wood platform on which environmental sensors are mounted.

A Young 81000 ultrasonic anemometer (Campbell Scientific, Logan, Utah, USA) is mounted on top of the 45 cm rod allowing measurements of wind velocity vector components and ultrasonic temperature at an approximate height of 1.55 m. The Young 81000 is capable of measuring wind velocity vector components up to 30 m s^{-1} with a resolution of 0.01 m s^{-1} and an accuracy of $\pm 1\% \text{ rms} \pm 0.01 \text{ m s}^{-1}$. Ultrasonic temperature measurements have a range from -50 to 50° C with a resolution of 0.01° C . Data is converted to an analogue signal between 0 and 5000 mV using a 12 bit DAC with an accuracy of $\pm 0.1\%$ of the measurements' full scale. The wind velocity vector component measurements were calibrated using a wind tunnel (Nambiar et al. 2020).

An HMP 60 temperature and relative humidity sensor (Vaisala, Helsinki, Finland) is mounted below the anemometer on the top rod. The temperature sensor is a 1000Ω platinum resistance thermometer with a measurement range of -40 to 60° C and an accuracy of $\pm 0.6^\circ \text{ C}$. Due to the thermal mass of the HMP60 sensor, thermal measurements would lag behind the true temperature, which may lead to inaccurate readings when used on a mobile platform. Therefore, the ultrasonic temperature is used for analysis throughout the rest of this paper.

The HMP60's INTERCAP relative humidity sensor has a range of 0 to 100% non-condensing with an accuracy of $\pm 3\%$ for relative humidities less than 90%. Data is encoded in a 0 to 1000 mV analogue signal. The ultrasonic temperature was used for all temperature analyses, but it was first calibrated using the HMP60 temperature sensor (Nambiar et al. 2020).

Environmental data is collected using the Campbell Scientific CR6 data logger due to its high accuracy and reliability. The 24-bit ADCs allow for lossless data transfer from the Young 81000 and HMP60 sensors at 10 Hz (Aliabadi et al. 2019, Aliabadi, Moradi, and Byerlay 2021). Collected data is stored on a microSD card every minute to reduce the risk of data loss. The CR6 is powered by the

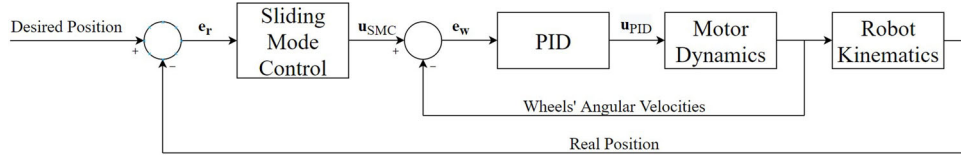


Fig. 3. Controller architecture for ARES.

12 V buck regulator which in turn provides regulated power to both instruments.

Control

Accurate positioning of the robot is key to taking reliable environmental measurements, therefore an accurate position controller was developed. Due to its simplicity, we employed a kinematic model of the robot for control development. The kinematic model of the robot is described as

$$\dot{\xi}_I = \mathbf{B}^{-1}(\theta)(r \cdot \mathbf{u} + \mathbf{v}_s), \quad (1)$$

where $\dot{\xi}_I = [\dot{x} \ \dot{y} \ \dot{\theta}]^T$ is the velocity of the robot, x , y , and θ are the global coordinates of the robot, r is the radius of each wheel, \mathbf{u} is the angular velocity of each wheel, \mathbf{v}_s is the linear slip velocity of each wheel, and

$$\mathbf{B}(\theta) = \begin{bmatrix} \sin\theta & -\cos\theta & -l \\ \frac{\sqrt{3}}{2}\cos\theta - \frac{1}{2}\sin\theta & \frac{\sqrt{3}}{2}\sin\theta + \frac{1}{2}\cos\theta & -l \\ -\frac{\sqrt{3}}{2}\cos\theta - \frac{1}{2}\sin\theta & -\frac{\sqrt{3}}{2}\sin\theta + \frac{1}{2}\cos\theta & -l \end{bmatrix}, \quad (2)$$

where l is the distance from the robot's center of rotation to each wheel. Using a kinematic model provides a distinct advantage over dynamic models, since the kinematic model is independent of load, allowing sensors to be added or removed from ARES without the need to re-tune the controller. The controller will only need to be re-tuned if the motors or the wheels' radii are changed.

Using the kinematic model, a sliding mode controller can be designed. We start by defining the sliding surface as

$$\sigma = \mathbf{e}_r + \lambda \int \mathbf{e}_r dt, \quad (3)$$

where σ is the sliding surface, $\lambda \in \mathbb{R}^{3 \times 3}$ is a positive design matrix, and $\mathbf{e}_r = \xi_I - \xi_d$ is the robot's positional error defined as the difference between the robot's real position, $\xi_I \in \mathbb{R}^{3 \times 1}$, and the robot's desired position, $\xi_d \in \mathbb{R}^{3 \times 1}$. The equivalent control portion of the input is defined by setting the derivative of the sliding surface to zero and solving for the control vector $\hat{\mathbf{u}}_{SMC}$ as

$$\dot{\sigma} = \dot{\mathbf{e}}_r + \lambda \mathbf{e}_r = \mathbf{B}^{-1}(\theta)(r \cdot \hat{\mathbf{u}}_{SMC} + \hat{\mathbf{v}}_s) - \dot{\xi}_d + \lambda \mathbf{e}_r, \quad (4)$$

$$\hat{\mathbf{u}}_{SMC} = \frac{1}{r} (\mathbf{B}(\theta)(-\lambda \mathbf{e}_r + \dot{\xi}_d) - \hat{\mathbf{v}}_s) \quad (5)$$

where $\hat{\mathbf{v}}_s \in \mathbb{R}^{3 \times 1}$ is a vector containing the estimated slip velocity of each wheel. Since ARES does not have any sensors for determining slip, it is assumed that $\mathbf{v}_s = 0$ and the error created by this is handled by the SMC.

To maintain the system on the sliding surface, the discontinuous portion of the controller is defined as

$$\mathbf{u}_{c,SMC} = -\mathbf{B}(\theta)\mathbf{k}\text{sign}(\sigma), \quad (6)$$

where $\mathbf{k} \in \mathbb{R}^{3 \times 3}$ is a positive definite design matrix and $\text{sign}()$ is the signum function. Combining (5) and (6), the complete controller is defined as

$$\mathbf{u}_{SMC} = \frac{1}{r} (\mathbf{B}(\theta)(-\lambda \mathbf{e}_r + \dot{\xi}_d)) - \mathbf{B}(\theta)\mathbf{k} \text{sign}\left(\mathbf{e}_r + \lambda \int \mathbf{e}_r \cdot dt\right). \quad (7)$$

The output of the SMC in (7) is the desired angular velocity of each wheel. Through trial and error, appropriate values for the design matrices were found to be

$$\lambda = \begin{bmatrix} 7 & 0 & 0 \\ 0 & 7 & 0 \\ 0 & 0 & 6 \end{bmatrix}, \quad (8)$$

$$\mathbf{k} = \begin{bmatrix} 0.01 & 0 & 0 \\ 0 & 0.01 & 0 \\ 0 & 0 & 0.01 \end{bmatrix}. \quad (9)$$

Although the signal of the SMC could be converted directly to a PWM signal to be sent to the motors, this will cause inaccurate control of the wheels' angular velocities. Instead, a Proportional-Integral-Derivative (PID) controller is applied to each motor, providing a faster and more accurate response to changes in \mathbf{u}_{SMC} . The PID controller for each wheel is expressed as

$$\mathbf{u}_{PID} = K_p \mathbf{e}_w + K_i \int_0^t \mathbf{e}_w dt + K_d \frac{d}{dt} \mathbf{e}_w \quad (10)$$

where K_p , K_i , and K_d are the proportional, integral, and derivative gains with the values of 10, 0.1, and 30, respectively, \mathbf{e}_w is angular velocity error, and \mathbf{u}_{PID} is the control effort, which ranges from 0 to 100% of the PWM signal. Figure 3 shows the controller architecture with an SMC for positional control and a PID acting as a sub-controller for the wheels.

Environmental sensing

The current configuration of the experimental platform is capable of measuring the relative humidity (RH), temperature (T), and wind velocity vector components (U , V , W along the x , y , and z directions, respectively). Wind velocity vector components and temperature are described using Reynolds decomposition as $X = \bar{X} + x$, where X is the measured variable, \bar{X} is the average of X , and x is the instantaneous variation of X . The covariance between variables X and Y over N measurements is described as

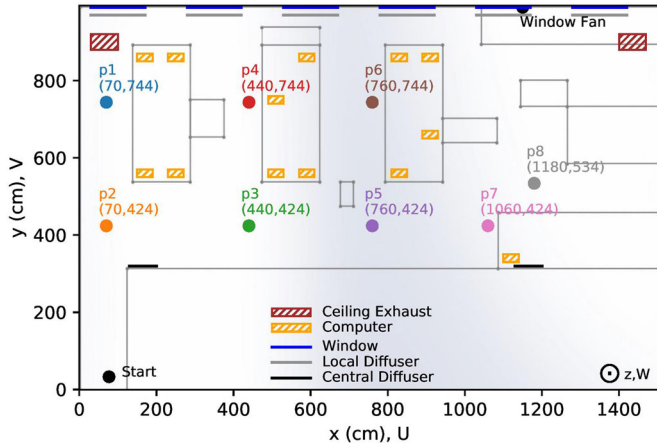


Fig. 4. Simplified model of the room with measurement positions.

$$\overline{xy} = \frac{1}{N} \sum_{i=1}^N (X_i - \bar{X})(Y_i - \bar{Y}) = \frac{1}{N} \sum_{i=1}^N x_i y_i, \quad (11)$$

while the variance of a single variable is simplified to $\overline{x^2} = \frac{1}{N} \sum_{i=1}^N x_i^2$.

For a set of N measurements, the systematic and random error of the measured variances and covariances can be calculated, respectively, as

$$SE = 2 \frac{\tau}{T}, \quad (12)$$

$$RE = \sqrt{2 \frac{\tau}{T}}, \quad (13)$$

where T is the total measurement period and τ is the integral time scale. The integral time scale can be calculated by integrating the cross-auto-correlation functions from a time shift of 0s to the time shift associated with the first zero-crossing of the function (Ahmadi-Baloutaki and Aliabadi 2021). The cross-auto-correlation function is formulated as

$$\hat{R}_{XY}(k) = \frac{\sum_{t=0}^{N-k-1} x_t y_{t+k}}{\left[\sum_{t=0}^{N-k-1} x_t y_t \right]^{1/2} \left[\sum_{t=0}^{N-k-1} x_{t+k} y_{t+k} \right]^{1/2}}, \quad (14)$$

where $\hat{R}_{XY}(k)$ is the cross-auto-correlation function and k is the measurement lag (Aliabadi et al. 2016). The auto-correlation function is found using (14) with X and Y expressing the same variable. Once the systematic and random errors are known, they can be used to correct the calculations of turbulence variances and covariances.

PMV-PPD model

The PMV-PPD model was developed by Fanger (1972) to estimate the average thermal comfort rating that a large group of subjects would experience. The model depends on physiological parameters (metabolic rate, M , and level of clothing) and environmental variables (ambient air temperature, T ; mean radiant temperature, \bar{T}_r ; wind speed, S ; and relative humidity, RH). Using these parameters, the thermal

load, L , on a subject's body is estimated, and the PMV is defined as

$$PMV = [0.303 \exp(-0.036M) + 0.028]L. \quad (15)$$

Using the PMV equation, the Predicted Percent Dissatisfied (PPD) is calculated as

$$PPD = 100 - 95 \exp[-(0.03353PMV^4 + 0.2179PMV^2)]. \quad (16)$$

By definition, the PPD can never be less than 5% and a PMV range of ± 0.5 corresponds to a PPD of 10%. The PMV-PPD model is defined in the ISO standard 7730 with a set of programs to aid in its calculation (ISO standard 2005).

The platform does not use a sensor for measuring the mean radiant temperature, but it uses the ambient air temperature as a proxy. This introduces an average systematic error of ± 0.3 K in estimating the mean radiant temperature (Dawe et al. 2020). This assumption introduces a small error which can be estimated by calculating the largest relative error in PMV and PPD using error propagation. A large error of 0.6 K in mean radiant temperature results in a relative PMV error of $\pm 10\%$ and a relative PPD error of $\pm 13\%$.

Environmental experiment

Measurements of the indoor environment were performed at the University of Guelph in Room 2510 of the Richards Building, a schematic of which is shown in Figure 4. The room is used as a lab, with twelve workstations outfitted with desktop computers. The workstations act as heat sources (occupants and computers) when in use, with most active during the day, and a few active overnight. The environment is regulated using a row of local diffusers along the outer wall (near windows). Each local diffuser is in front of a window, pulling air from ground level and pushing air straight up from 1.2 m above the ground. Two central diffusers are located above the inner wall, and exhausts are in the ceiling closer to the outer wall.

Lab members have found the lab to be uncomfortably warm in the early to mid-afternoon of the summer/fall seasons. To combat this, a fan has been placed in front of a slightly ajar window, blowing over a local diffuser, and the fan runs day and night, cooling the room to a more comfortable level. The room temperature was set to a desired value of 18.5°C and a relative humidity of 30% during the experiment.

Measurements were taken at eight positions around the room, labeled as p1-8 in Figure 4. Positions 1, 4, 6, and 7 were chosen due to their proximity to the workstations. At these positions it is assumed that personnel are seated and typing, resulting in a low metabolism of 1.1 met. Positions 2, 3, 5, and 8 are near a white board and are on the main walkway of the room; therefore, at these positions it is assumed that members are standing and writing, or walking at a leisurely pace, increasing metabolic rate to 1.7 met. The start position is located at the entrance of the room and allowed the robot to be pushed up against the door to ensure

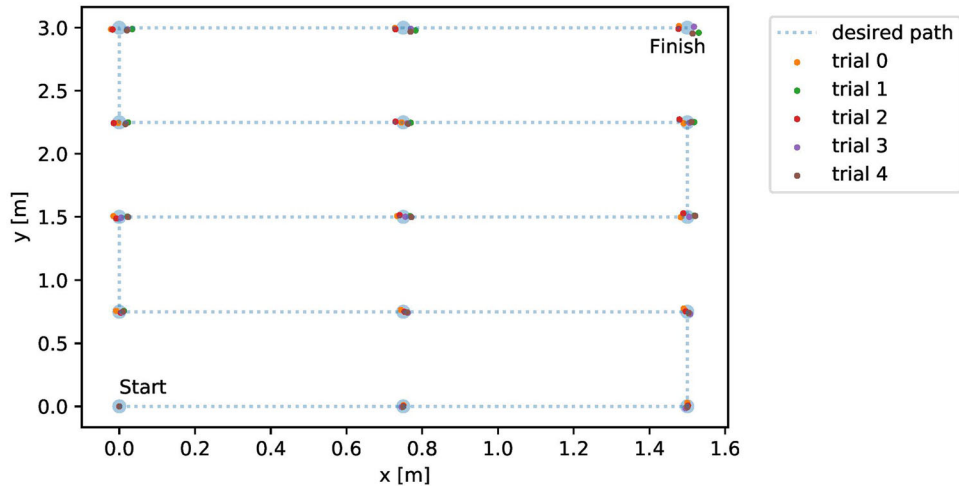


Fig. 5. Position of robot at each test point over the path, moving in the positive y direction.

its proper angular alignment. Without this alignment, the robot is prone to drift since it has no vision system to determine the starting angular bias.

Testing was conducted by having the robot navigate between the positions sequentially. Data was collected for 160 seconds at 10 Hz at each position. This resulted in a runtime of 24 minutes to measure the whole room's environmental variables. Testing was carried out over two periods with runs starting every half hour. The first period started at 1530 Eastern Daylight Time (EDT) on October 2, 2020 and lasted until 1000 EDT on October 3, 2020. The second period started at 0800 EDT on October 8, 2020 and lasted until 1530 EDT of the same day. Data from the first period, from 1530 until 0800, was combined with all the data from the second period resulting in the measurement of a full diurnal cycle.

The path the robot followed was generated using a D*-lite path planning algorithm which was adapted from Koenig and Likhachev (2002). The D*-lite algorithm was chosen due to its fast-computational time and the ability to later apply the same path planning algorithm to dynamic and unmapped environments. A map of the room was generated from Figure 4 by expanding the perimeter of all obstacles by 40 cm, allowing the path generated to keep the robot far from any obstacles. The path was modified to ensure the robot would not attempt to move faster than it is capable, improving its positional reliability. The path was sent to the robot using the xBee communication module and the position of the robot was stored on a computer. An experimenter was present during the tests to ensure the robot remained on the desired path and reached measurement points accurately.

During the run starting at 1930 EDT the robot ran into a chair which had been placed in its path by accident. This interference stopped the robot from reaching positions 3 and 4 accurately; therefore, these positions are excluded from analysis at 1930 EDT.

Results and discussion

Controller performance verification

Prior to environmental testing, the developed control scheme was verified over long-distance trajectories. This was performed to quantify expected errors, which commonly arises due to drift and should be compensated for to increase the controller's accuracy.

Verification of the controller was performed by having the robot execute a square-wave pattern, as seen in Figures 5 and 6. The square-wave pattern consisted of 15 points each positioned 0.75 m from the previous point. To simulate an environmental sensing experiment, the robot was planned to arrive at a full stop at each point. Back and forth motion allows drift to eliminate itself, and thus we calculated it only in the direction where the robot moves without back tracking. The robot was tested translating in the positive x and y directions 5 times each and the results were averaged for the calculation of drift. The data was collected using a VICON tracking system that measures position at 50 Hz with a resolution of 0.1 mm. The drift of the robot in the x -direction is 2.9 mm m^{-1} and in the y -direction is 2.0 mm m^{-1} .

The Root Mean Square Error (RMSE) of the robot position was determined using a four-petal parametric rose trajectory, shown in Figure 7, and defined as

$$\begin{bmatrix} x \\ y \\ \theta \end{bmatrix} = \begin{bmatrix} \cos\left(\frac{\pi t}{15}\right) \cos\left(\frac{\pi t}{30}\right) \\ \sin\left(\frac{\pi t}{15}\right) \cos\left(\frac{\pi t}{30}\right) \\ 0 \end{bmatrix}. \quad (17)$$

Since the rose is symmetric, drift is minimized allowing calculation of the RMSE. The RMSE of the robot is 4.1 mm in the x direction and 4.3 mm in the y direction. These RMSEs and drifts are deemed acceptable for indoor environmental sensing. The RMSE in angular position is 0.5

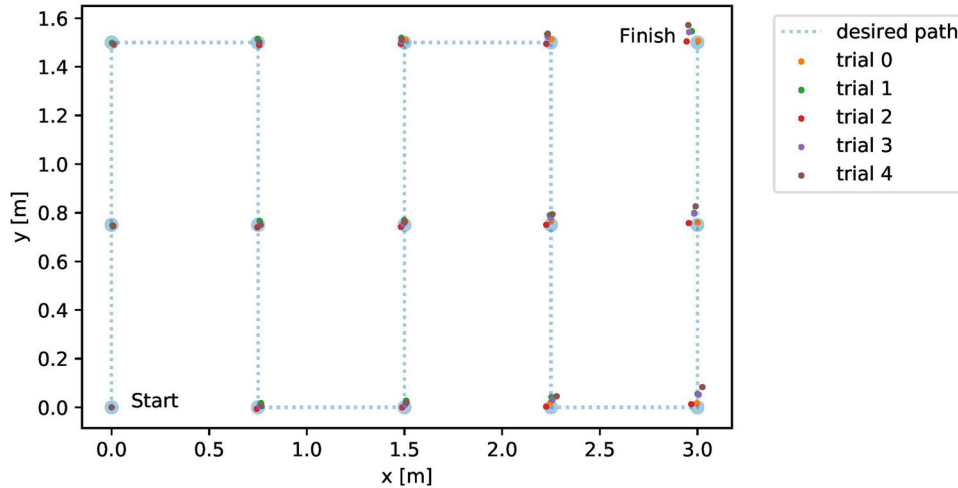


Fig. 6. Position of robot at each test point over the path, moving in the positive x direction.

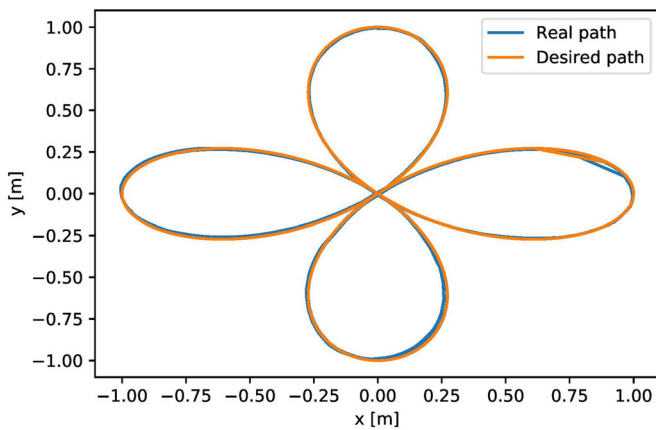


Fig. 7. Real and desired paths of ARES using a sliding mode controller with PIDs on each wheel.

degrees, which while small, is the greatest contributor to drift. Since the robot uses low-cost DC motors, the wheel axle can rotate a small amount without being detected by the encoders. This allows the robot to rotate slightly without the controller noticing, causing higher drift and RMSE. For the purposes of these experiments, the platform's capabilities are adequate; however, the use of higher precision DC motors or a gyroscope for sensing rotation would increase accuracy allowing for larger indoor spaces to be explored.

Environmental statistics

The positional and environmental data were combined into a large dataset, with which all statistics and PMV-PPD values were calculated. The most important variables among these statistics are the average total wind speed, average temperature, average relative humidity, vertical turbulent sensible kinematic heat flux, and the turbulence kinetic energy, all of which are discussed below. The systematic errors associated with variances and co-variances were calculated and the data was corrected for these errors by multiplying the associated

variances or co-variances by $1 + SE$. Random errors are not plotted for brevity of presentation.

The average wind speed, \bar{S} , is shown in Figure 8a. As can be seen from the plot, most of the room has slow moving air at less than 0.1 m s^{-1} . The average wind speed at position 8 is significantly higher than the rest of the room since it is directly in the path of the window fan. During the day, the wind speed at position 8 is significantly lower than during the evening and overnight due to the Heating Ventilation and Air Conditioning (HVAC) system schedule. The HVAC system pushes air up through the local diffuser which interferes with the air stream from the fan causing turbulence and a reduction in total average wind speed. At night, the HVAC system is turned off allowing the fan to push air uninterrupted toward the platform resulting in higher wind speed measurements. Position 8 experiences higher average wind speeds, compared to other positions, during the day due to the interaction between the fan and HVAC system causing the moving air to spread out more.

Position 4 shows raised wind speed due to a computer near it producing a thermal plume. The heat from the computer causes a rising column of warm air to form, increasing the average wind speed. This is confirmed by a higher-than-average co-variance between the z-direction wind velocity vector component, W , and ambient air temperature, T , shown in Figure 8b, and a higher-than-average temperature when compared to the rest of the room, as can be seen in Figure 8c.

Temperatures in the room exhibit a strong diurnal cycle, warming in the morning starting at 0700 EDT and cooling in the evening, starting around 1700 EDT. The drop in temperatures at 1530 EDT is due to the measurements spanning two days, not due to room operations. During these tests, the HVAC system was set to cool the building, however, the fan near the window caused the room's temperature to drop below the building average temperature during the night influencing the HVAC system to equalize the temperature when it turned on at 0700 EDT. When the HVAC system turned off in the evening, the window fan was able to cool

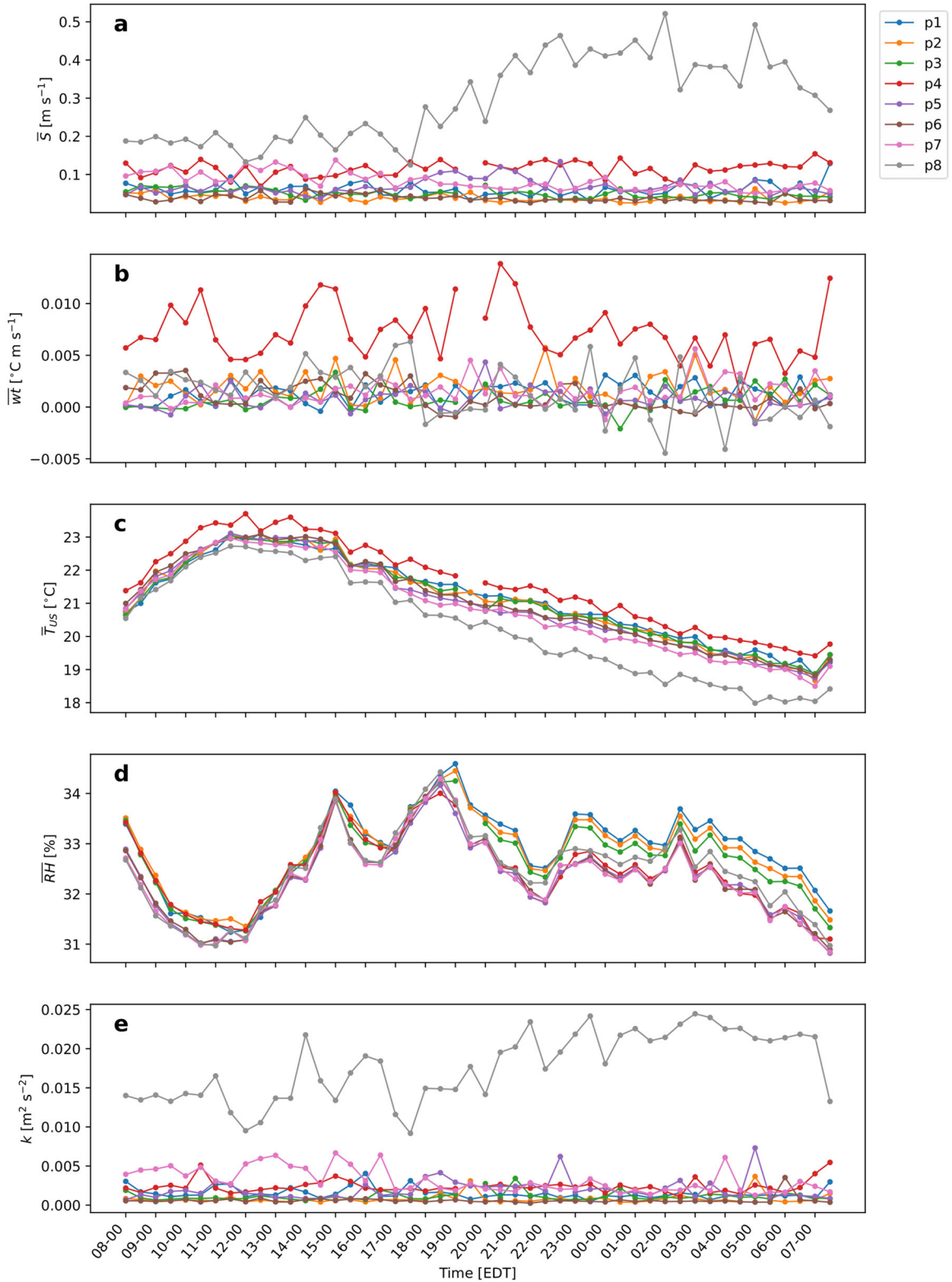


Fig. 8. Environmental Statistics over a diurnal cycle. (a) average wind speed, (b) covariance between z-direction wind velocity vector component and temperature, (c) average ultrasonic temperature, (d) average relative humidity, (e) turbulent kinetic energy.

the room down using air from outside. As expected, position 8 is the coolest due to being directly in the path of the fan. The temperature slowly increased at positions farthest from the fan, indicating a horizontal temperature gradient as high

as 0.1 K m^{-1} . The notable exception is position 4 which is warmer than the rest of the room due to an active computer.

The average relative humidity, shown in Figure 8d, remained constant throughout testing. During the warming

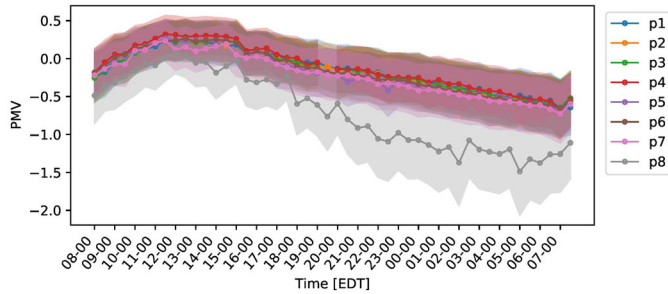


Fig. 9. PMV at all positions with a metabolic rate of 1.4 met and clothing levels ranging from 0.57 clo to 0.96 clo (represented by the color band). Data points correspond to a clothing level of 0.74 clo.

period, the relative humidity dropped by 2% since, using psychrometric considerations, a rise in temperature causes a drop in relative humidity. After 1200 EDT, the relative humidity rises back to approximately 33% as the room balances with the rest of the building through the HVAC system. During the night, there is a divergence as positions closer to the window have lower relative humidity, likely due to lower relative humidity outside. Position 1 has the highest average relative humidity due to the experimenter sitting at a workstation approximately 1 meter from the sensors.

The turbulence kinetic energy (TKE) is shown in Figure 8e. As shown, most of the measured points in the room have low TKE, less than $0.005 \text{ m}^2 \text{ s}^{-2}$, indicating lower levels of turbulence, however position 8 has a significantly higher TKE, around $0.015 \text{ m}^2 \text{ s}^{-2}$, during the day and rising to nearly $0.025 \text{ m}^2 \text{ s}^{-2}$ overnight. The rise in TKE in the evening supports the hypothesis that the HVAC system interferes with airflow from the fan and spreads it out, reducing the TKE. In the evening, the lack of forced air from the HVAC system allowed the highly turbulent airflow from the fan to reach position 8 resulting in a higher TKE.

Thermal comfort

Thermal comfort was evaluated at three different clothing levels and two metabolic rates. Since these tests were performed in the fall, clothing levels were chosen to represent normal wear during the time of the year. The base case used a clothing level of 0.74 clo corresponding with wearing trousers and a long sleeve sweater with socks and shoes. The high case used a clothing level of 0.96 clo corresponding with wearing trousers, a long sleeve shirt, and a jacket with socks and shoes. The low case used a clothing level of 0.57 clo corresponding with wearing trousers and a short sleeve shirt with socks and shoes. For brevity, all positions were evaluated at a metabolic rate of 1.4 met, corresponding to a mix state of working at a desk and light activity moving about the laboratory.

The PMV at each position is shown in Figure 9. The room tends to be slightly cool in the morning and slightly warm in the afternoon. Position 8 has a lower PMV than the other three positions due to high wind speed causing draft;

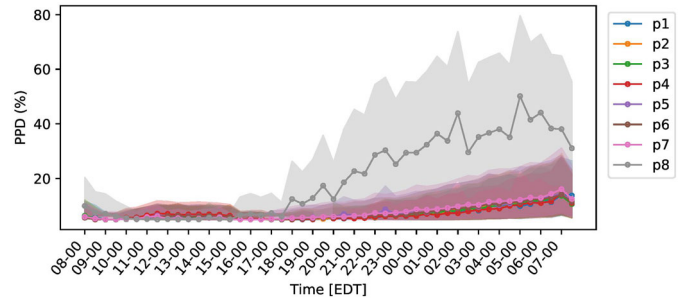


Fig. 10. PPD at all positions with a metabolic rate of 1.4 met and clothing levels ranging from 0.57 clo to 0.96 clo (represented by the color band). Data points correspond to a clothing level of 0.74 clo.

however, it remains above a PMV of -1 even when wearing light clothing during the day, only dropping to uncomfortably cold levels overnight where the lab is not in use. PPD for these positions is shown in Figure 10. During the day, the PPD at all positions is less than 10% except at position 8, where in the first and last hour of the work day, the PPD rises above 10% when wearing light clothes. Between 1200 and 1600, the PPD is above 5% due to the room being warm; however, this allows the PPD to remain below 10% throughout the room for longer. PPD remains below 25% throughout the night at all but position 8, which has a significantly higher PPD due to cool air being pulled in from outside at higher-than-average wind speeds, causing a cool draft.

From this analysis, the ARES platform can measure an environment and quantify its thermal comfort level. With minor modifications the platform can run completely autonomously, without the need to change batteries or reset its position for each measurement period. Data collected by the platform can be used to better inform building design for thermal comfort and identify areas of large buildings that need to have their environmental variables adjusted.

Platform viability

The greatest advantages that ARES provides over other methods of environmental sensing are its cost-effectiveness and ease of use. Compared to static sensors, ARES is significantly more economical as it can measure multiple locations with a single set of sensors. The total cost of ARES is \$800 USD plus the cost of any sensors used. Given the experimental configuration in this study, each set of sensors (a Young 81000 ultrasonic anemometer, an HMP60 relative humidity and temperature sensor, and a CR6 datalogger) costs approximately \$6000 USD. When combined with the ARES platform, the total cost to monitor 8 positions is approximately \$6800 USD, while the cost to set up a sensor station at each position measured in this study will be approximately \$48,000 USD. In its current configuration, ARES is cost-effective even when measuring only two positions.

To increase measurement accuracy, it is important to minimize systematic errors when measuring turbulence statistics. While an acceptable level of systematic error must be

determined on a case-by-case basis, a 10% error is acceptable for the experiment described. According to (12), a 10% systematic error requires the integral time scale to be $1/20^{\text{th}}$ the sampling period's length. For the experimental run in this study, the sampling time was set to 160 s, causing the systematic error to be 10% or lower when the integral time scale is 8 s or less. Over the 3840 calculated time scales, 83% are 8 s or lower. In addition, 94% of measurements have a systematic error of less than 20%, corresponding to an integral time scale of 16 s or less.

When measuring turbulence statistics, the sampling time for ARES should be chosen based on the acceptable level of systematic error and the number of positions to be sampled over the desired period. More positions can be sampled at the cost of a higher systematic error, or systematic error at each position can be minimized by measuring fewer positions for longer periods of time. For the experimental run in this study, collecting a set of data every hour instead of every half hour would allow for a measurement period of 360 s, causing the systematic error to be lower than 10% for 95% of measurements.

The platform's mobile feature allows for previously-difficult or impossible measurements to be made without significant changes to the environment. For example, static sensors cannot take measurements in high traffic areas near ground level due to interference with foot traffic. However, if the space is only high traffic during specific times, for example the hallways of a school, ARES can move into position, take measurement, and move out of the way to avoid interfering with occupants.

Conclusion and future work

In this paper, a thermal comfort measurement and quantification system was developed and tested. To collect data on the indoor environment, the Autonomous Robotic Environmental Sensor (ARES) was developed, which uses a custom-designed omniwheel robot base and a sliding mode controller based on the platform's kinematic model to produce a mobile platform with high positional accuracy. The robot's modular design allows implementing a variety of sensors. For the experiments in this study, a Young 81000 ultrasonic anemometer and an HMP60 sensor were used to measure the wind velocity vector, temperature, and relative humidity. The indoor environment in a lab at the University of Guelph was investigated using the ARES by taking measurements at eight positions about the room every half hour over a 24-hour period in fall 2020.

Verification of the controller for the ARES revealed a position RMSE of 0.4 mm and a maximum drift of 2.0 mm m^{-1} in the x-direction and 2.9 mm m^{-1} in the y-direction. Collected environmental data was used to calculate averages, variances, and co-variances of thermo-fluid variables at each position, providing insight on the room's physical environment. The Predicted Mean Vote (PMV) and the Predicted Percent Dissatisfied (PPD) were calculated for each position showing that the room was comfortable during the day, but

areas of the room became uncomfortable during the evening and overnight, depending on clothing level. These results show that the ARES platform can perform its intended tasks with little human intervention, making it ideal for long term measurements of the indoor environment.

In the future, implementation of a Light Detection And Ranging (LIDAR) system for obstacle avoidance and localization would allow the robot to operate completely autonomously. A LIDAR system would also allow the robot to operate in a cluttered environment around humans without concern of running into objects or people, and always reach the desired position accurately. Additionally, more environmental sensors can be added to the robot to measure mean radiant temperature, particulate concentrations, gaseous contaminants, noise levels, or any other variable that affects indoor environmental quality.

Disclosure statement

No potential conflict of interest was reported by the author(s).

Funding

This work was supported by the Discovery Grant program (400911, 401231) from the Natural Sciences and Engineering Research Council (NSERC) of Canada. The lead author was partially funded by the University of Guelph.

ORCID

Amir A. Aliabadi  <http://orcid.org/0000-0002-1002-7536>

References

- Ahmadi-Baloutaki, M., and, A. A. Aliabadi. 2021. A very large-eddy simulation model using a reductionist inlet turbulence generator and wall modelling for stable atmospheric boundary layers. *Fluid Dynamics* 56 (3):413–32. doi:10.1134/S0015462821020026
- Aliabadi, A. A., M. Moradi, and R. A. E. Byerlay. 2021. The budgets of turbulence kinetic energy and heat in the urban roughness sublayer. *Environmental Fluid Mechanics* 21 (4):843–84. doi:10.1007/s10652-021-09800-x
- Aliabadi, A. A., M. Moradi, D. Clement, W. D. Lubitz, and B. Gharabaghi. 2019. Flow and Temperature Dynamics in an Urban Canyon Under a Comprehensive Set of Wind Directions, Wind Speeds, and Thermal Stability Conditions. *Environmental Fluid Mechanics* 19 (1):81–109. doi:10.1007/s10652-018-9606-8
- Aliabadi, A. A., S. N. Rogak, K. H. Bartlett, and S. I. Green. 2011. Preventing airborne disease transmission: review of methods for ventilation design in health care facilities. *Advances in Preventive Medicine* 2011:124064. doi:10.4061/2011/124064
- Aliabadi, A. A., R. M. Staebler, M. Liu, and A. Herber. 2016. Characterization and parametrization of reynolds stress and turbulent heat flux in the stably-stratified lower arctic troposphere using aircraft measurements. *Boundary-Layer Meteorology* 161 (1):99–126. doi:10.1007/s10546-016-0164-7

- Aliabadi, A. A., N. Veriotes, and G. Pedro. 2018. A very large-eddy simulation (VLES) model for the investigation of the neutral atmospheric boundary layer. *Journal of Wind Engineering and Industrial Aerodynamics* 183:152–71. doi:10.1016/j.jweia.2018.10.014
- ASHRAE. 2017. *ASHRAE handbook - fundamentals*. Peachtree Corners, GA: American Society for Heating, Refrigerating, and Air Conditioning Engineers (ASHRAE) Headquarters.
- Bi, S., D. Yang, and Y. Cai. 2018. Automatic calibration of odometry and robot extrinsic parameters using multi-composite-targets for a differential-drive robot with a camera. *Sensors (Switzerland)* 18 (9):3097. doi:10.3390/s18093097
- Caubel, J. J., T. E. Cados, and T. W. Kirchstetter. 2018. A new black carbon sensor for dense air quality monitoring networks. *Sensors (Switzerland)* 18 (3):738. doi:10.3390/s18030738
- Chen, Y., H. Cai, Z. Chen, and Q. Feng. 2017. Using multi-robot active olfaction method to locate time-varying contaminant source in indoor environment. *Building and Environment* 118:101–12. doi:10.1016/j.buildenv.2017.03.030
- Dawe, M., P. Raftery, J. Woolley, S. Schiavon, and F. Bauman. 2020. Comparison of mean radiant and air temperatures in mechanically-conditioned commercial buildings from over 200,000 field and laboratory measurements. *Energy and Buildings* 206:109582. doi:10.1016/j.enbuild.2019.109582
- Fan, Y. 2019. Performance evaluation of different air distraction system on thermal uniformity and energy saving: a case study of a Japanese detached house. *Indoor and Built Environment* 28 (2): 186–94. doi:10.1177/1420326X18790311
- Fanger, P. O. 1972. Thermal comfort: analysis and applications in environmental engineering. *Applied Ergonomics* 3 (3):181. doi:10.1016/S0003-6870(72)80074-7.
- Feng, Q., C. Zhang, J. Lu, H. Cai, Z. Chen, Y. Yang, F. Li, and X. Li. 2019. Source localization in dynamic indoor environments with natural ventilation: an experimental study of a particle swarm optimization-based multi-robot olfaction method. *Building and Environment* 161:106228. doi:10.1016/j.buildenv.2019.106228
- Földváry Licina, V., T. Cheung, H. Zhang, R. de Dear, T. Parkinson, E. Arens, C. Chun, S. Schiavon, M. Luo, G. Brager, et al. 2018. Development of the ASHRAE global thermal comfort database II. *Building and Environment* 142:502–12. doi:10.1016/j.buildenv.2018.06.022
- Gärtner, J. A., F. Massa Gray, and T. Auer. 2020. Assessment of the impact of HVAC system configuration and control zoning on thermal comfort and energy efficiency in flexible office spaces. *Energy and Buildings* 212:109785. doi:10.1016/j.enbuild.2020.109785
- Heinzerling, D., S. Schiavon, T. Webster, and E. Arens. 2013. Indoor environmental quality assessment models: a literature review and a proposed weighting and classification scheme. *Building and Environment* 70:210–22. doi:10.1016/j.buildenv.2013.08.027
- ISO standard. 2005. *ISO 7730:2005(En) Ergonomics of the thermal environment - analytical determination and interpretation of thermal comfort using calculation of the PMV and PPD indices and local thermal comfort criteria*. Geneva, Switzerland: International Organization for Standardization ISO Central Secretariat.
- ISO standard. 2017. *ISO-21748: guidance for the use of repeatability, reproducibility and trueness estimates in measurement uncertainty evaluation*. Geneva, Switzerland: International Organization for Standardization ISO Central Secretariat.
- Jin, M., S. Liu, S. Schiavon, and C. Spanos. 2018. Automated mobile sensing: towards high-granularity agile indoor environmental quality monitoring. *Building and Environment* 127:268–76. doi:10.1016/j.buildenv.2017.11.003
- Koenig, S., and M. Likhachev. 2002. D* Lite. In Proceedings of the National Conference on Artificial Intelligence, Edmonton, AB, July 28 - August 2, 476–83.
- Lee, S., D. Lee, P. Choi, and D. Park. 2020. Accuracy–power controllable lidar sensor system with 3D object recognition for autonomous vehicle. *Sensors (Switzerland)* 20 (19):5706. doi:10.3390/s20195706
- Lilienthal, A. J., A. Loutfi, and T. Duckett. 2006. Airborne chemical sensing with mobile robots. *Sensors (Switzerland)* 6 (11):1616–78. doi:10.3390/s6111616
- Nambiar, M. K., Byerlay, R. A., Nazem, A., Nahian, M. R., Moradi, M., & Aliabadi, A. A. (2020). A tethered air blimp (TAB) for observing the microclimate over a complex terrain. *Geoscientific Instrumentation, Methods, and Data Systems* 9 (1): 193–211. doi:10.5194/gi-9-193-2020
- Nielsen, P. V. 2015. Fifty years of CFD for room air distribution. *Building and Environment* 91:78–90. doi:10.1016/j.buildenv.2015.02.035
- Phillis, Y. 2008. Practical and experimental robotics, – Ferat Sahin and Pushkin Kachroo, (CRC Press 2007). Reviewed by Nikos Vlassis. *Journal of Intelligent and Robotic Systems* 52 (1):3. doi: 10.1007/s10846-008-9208-7
- Posner, J. D., C. R. Buchanan, and D. Dunn-Rankin. 2003. Measurement and prediction of indoor air flow in a model room. *Energy and Buildings* 35 (5):515–526. doi:10.1016/S0378-7788(02)00163-9
- Rabinovitch, N., C. D. Adams, M. Strand, K. Koehler, and J. Volckens. 2016. Within-microenvironment exposure to particulate matter and health effects in children with asthma: a pilot study utilizing real-time personal monitoring with GPS interface. *Environ Health* 15 (1):96. doi:10.1186/s12940-016-0181-5
- Reena, K. E. M., A. T. Mathew, and L. Jacob. 2018. A flexible control strategy for energy and comfort aware HVAC in large buildings. *Building and Environment* 145:330–342. doi:10.1016/j.buildenv.2018.09.016
- Schlink, U., and M. Ueberham. 2021. Perspectives of individual-worn sensors assessing personal environmental exposure. *Engineering* 7 (3):285–289. doi:10.1016/j.eng.2020.07.023
- Shan, X., and W.-Z. Lu. 2021. An integrated approach to evaluate thermal comfort in air-conditioned large-space office. *Science and Technology for the Built Environment* 27 (4):436–50. doi:10.1080/23744731.2020.1796420
- Smith, T. R., B. Thompson, J. Balfour, and A. Taher. 2020. Modular End-effector on mobile robot with automated change station. In 2020 4th International Conference on Robotics and Automation Sciences (ICRAS), Chengdu, China, 14 - 16 June, 2020, 34–38. IEEE. doi:10.1109/ICRAS49812.2020.9134921
- Williams, D. E. 2019. Low cost sensor networks: how do we know the data are reliable? *ACS Sensors* 4 (10):2558–65. doi:10.1021/acssensors.9b01455
- Wilson, E. K. 2019. Wearable sweat sensors. *Engineering* 5 (3): 359–60. doi:10.1016/j.eng.2019.04.008
- Yang, Y., Q. Feng, H. Cai, J. Xu, F. Li, Z. Deng, C. Yan, and X. Li. 2019. Experimental study on three single-robot active olfaction algorithms for locating contaminant sources in indoor environments with no strong airflow. *Building and Environment* 155:320–33. doi:10.1016/j.buildenv.2019.03.043
- Zhao, B., X. Li, and Q. Yan. 2003. A simplified system for indoor airflow simulation. *Building and Environment* 38 (4):543–52. doi: 10.1016/S0360-1323(02)00182-8